Internal Conversion of the Anionic GFP Chromophore: In and Out of the I-twisted S_1/S_0 Conical Intersection Seam

Nanna H. List, Chey M. Jones and Todd J. Martínez[*]

Department of Chemistry and The PULSE Institute, Stanford University, Stanford, CA 94305

SLAC National Accelerator Laboratory, 2575 Sand Hill Road, Menlo Park, CA 94025

[*]toddjmartinez@gmail.com

Abstract:
The functional diversity of the green fluorescent protein (GFP) family is intimately connected to the interplay between competing photo-induced transformations of the chromophore motif, anionic p-hydroxybenzylidene-2,3-dimethylimidazolinone (HBDI⁻). Its propensity to undergo Z/E photoisomerization following excitation to the $S_1(\pi\pi^*)$ state is of particular importance for super-resolution microscopy and emerging opportunities in optogenetics. However, key dynamical aspects of this process and its range of tunability still remain elusive. Here, we investigate the internal conversion behavior intrinsic to HBDI⁻ with focus on competing deactivation pathways, rate and yield of photoisomerization. Based on non-adiabatic dynamics simulations, we confirm that non-selective progress along the two bridge-torsional (i.e., phenolate, P, or imidazolinone, I) pathways can account for the three decay constants reported experimentally, leading to competing ultrafast relaxation along the I-twisted pathway and S_1 trapping along the P-torsion. The majority of the population (~70%) is transferred to S_0 in the vicinity of two near-symmetry-related minima on the I-twisted intersection seam (MECI-Is). Despite their reactant-biased topographies, our account of inertial effects suggests that isomerization not only occurs as a thermal process on the vibrationally hot ground state but also as a direct photoreaction with a total quantum yield of ~40%. By comparing the non-adiabatic dynamics to a photoisomerization committor analysis, we provide a detailed mapping of the intrinsic photoreactivity and dynamical behavior of the two MECI-Is. Our work offers new insight into the internal conversion process of HBDI⁻ that enlightens principles for the design of chromophore derivatives and protein variants with improved photoswitching properties.

Introduction

The green fluorescent protein (GFP[1-4]) and its relatives have established themselves as key tools in bioimaging and cell biology by enabling visualization of processes in realistic environments.[5-8] GFP proteins display a remarkable variety in photophysical properties, including spectral range, fluorescence quantum yield, photostability and photoswitchability.[9-12] Intriguingly, this functional diversity is enabled by relatively minor variations in the chromophore motif and/or the protein scaffold.[13-17] The function of these proteins is inextricably linked to the properties of the 4-hydroxybenzylidene-2,3-dimethylimidazolinone (HBDI$^-$) chromophore core[18] (Figure 1a).

Outside the protein environment (vacuum and in solution), the HBDI$^-$ chromophore is essentially non-fluorescent at room temperature, quenched by ultrafast radiationless decay.[19] In solution, fluorescence can be recovered at lowered temperatures by thermally- or weakly friction-controlled suppression of the internal conversion.[20-21] Using a combination of a femtosecond pump–probe scheme and a time-resolved action technique (detection of neutral fragments), Andersen and coworkers recently demonstrated fluorescence as an intrinsic property of the HBDI$^-$ chromophore.[22] Specifically, upon cooling to 100 K, the existence of tiny barriers on $S_1(\pi\pi^*)$ was demonstrated by trapping the isolated chromophore on the excited state for 1.2 ns, long enough to establish fluorescence conditions.

In the gas phase, the main deactivation pathways following photoexcitation to S_1 include internal conversion to the hot electronic ground state and electron autodetachment from the S_1 state to give the neutral HBDI radical in the D_0 state. With a vertical excitation energy of 2.57 eV,[23] the S_1 state of the isolated chromophore is bound with respect to vertical and adiabatic electron detachment (2.68±0.1,[24] 2.73±0.1,[10] 2.8±0.1[25] and 2.85±0.1[26] eV). Within a linear excitation regime, internal conversion is the dominant deactivation channel across the S_0–S_1 absorption band (415-500 nm),[27] while autodetachment plays a minor role (occurs on a ~30 ps time scale), as measured by direct electron detection.[28] According to time-resolved photoelectron (TRPES)[29] and action spectroscopy,[22] the excited-state population decay at room temperature is characterized by three time scales; a fast (~330 fs), an intermediate (1.3-1.4 ps) and a longer-lived component (>10 ps). However, the dominant decay mechanisms in operation remain unresolved experimentally because of the difficulties associated with differentiating the transient species.

Theoretical studies suggest that the excited-state decay proceeds along two alternative pathways, corresponding to rotation around one of the methine bridge bonds (i.e., either the

imidazolinone, I, or phenolate, P), and is accompanied by twisted intramolecular charge-transfer (TICT) across the bridge (Figure 1a). The coupling between torsion and charge-transfer is a common feature of monomethine dyes of which HBDI⁻ represents an asymmetric example near the so-called cyanine limit (i.e., characterized by the electronic charge being fully delocalized over the π-conjugated skeleton in the electronic ground state).[30-32] Importantly, the two different pathways in the anionic form feature oppositely directed charge transfer,[33-34] and only internal conversion about the I-bond may lead to direct photoisomerization whereas rotation around the P-bond recovers the original ground state (possibly the indistinguishable P-flipped configuration). So far, electronic structure methods capable of describing the energetic ordering of the I- and P-twisted configurations on S_1 of isolated HBDI⁻ have been limited to static calculations, providing valuable information about the potential energy landscape.[33,35] In particular, more recent high-level calculations confirm the existence of a shallow planar minimum on S_1 (~0.1 eV below the Franck–Condon (FC) point), characterized by elongated bridge bonds and similar bridge torsional barriers of ~0.05 eV.[35] However, due to the non-equilibrium conditions following photoexcitation, inertial effects are essential to address the dynamical importance of the alternative deactivation pathways as well as the intrinsic reactivity of the I-twisted channel. Recently, Carrascosa *et al.* employed a combination of tandem ion mobility mass spectrometry and laser spectroscopy to provide the first experimental evidence that isomerization is indeed an intrinsic response of HBDI⁻ upon photoexcitation.[27] However, the experiments were inconclusive as to whether isomerization is mediated directly by the internal conversion process or indirectly by subsequent torsional barrier crossing on the vibrationally hot ground state.

Here, we investigate the competition between the I- and P-deactivation pathways upon photoexcitation of isolated HBDI⁻ by performing non-adiabatic dynamics simulations using *ab initio* multiple spawning[36-37] (AIMS). In particular, we address the extent to which internal conversion is accompanied by photoisomerization and the factors determining the dynamical behavior of the system by comparing the dynamics results to a committor analysis of the accessed regions of the I-twisted intersection seam. Although intramolecular redistribution of the excess vibrational energy will eventually decide the fate of the gaseous hot electronic ground state (including thermal isomerization, photofragmentation and thermionic emission[23, 25, 27-28, 38]), the intrinsic photoresponse of the chromophore serves as a natural reference point to propose design strategies for HBDI⁻ systems with tailored photoactive properties.
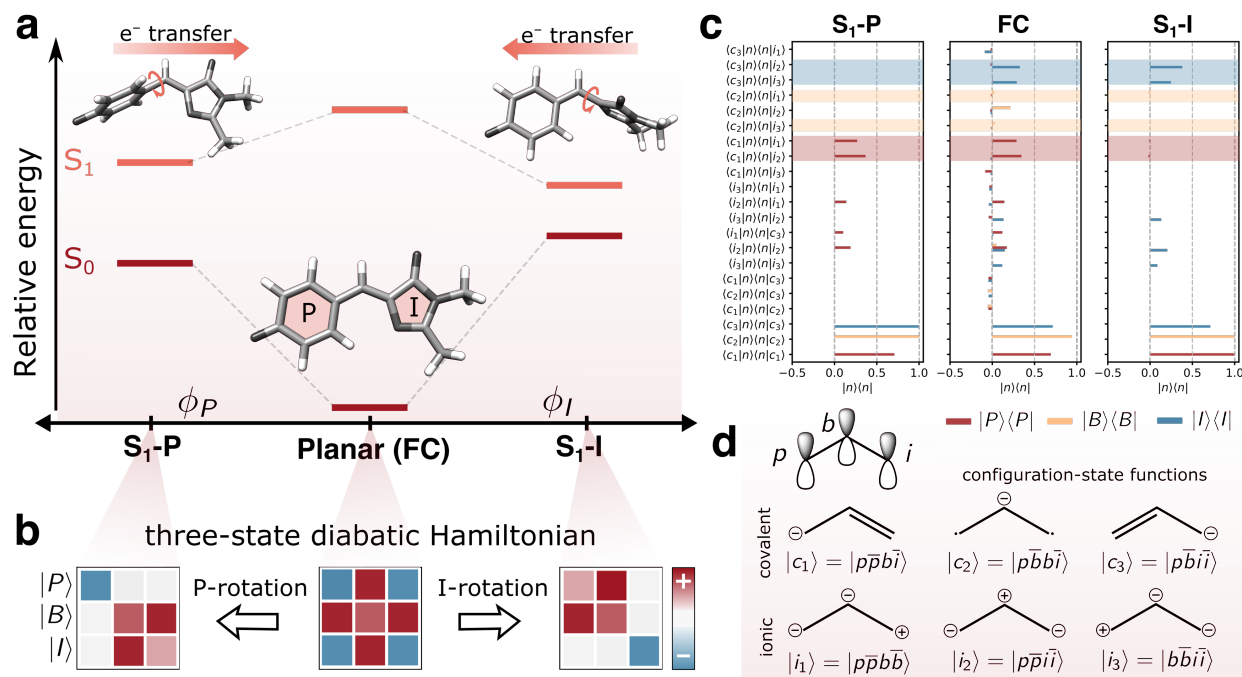
Figure 1. Coupling between bridge-torsional motion and intramolecular charge-transfer character in gaseous HBDI⁻. (a) Torsional dependence of the S_0 and S_1 energies and the direction of intramolecular charge-transfer on S_1, computed at the $\alpha(0.64)$-SA3-CASSCF(4,3)/6-31G* level. Underlying adiabatic state energies and Mulliken charges are reported in Tables S1-2 and definitions of key geometric parameters in Figure S1. (b) Schematic representation of the three-state diabatic Hamiltonian and how it changes upon bridge-torsional deformations.[39] Displacement along the torsional coordinates leads to a block-diagonal form. The colored shadings indicate the relative sign and magnitude of the matrix elements. (c) Decomposition of the diabatic states in terms of underlying CSFs, see (d). Within this orthonormalized fragment-localized basis, bond formation is a consequence of coupling between a covalent configuration and its corresponding bond-polarizing ionic configurations (the color-coding of the shaded areas highlights the stabilizing ionic contributions to each diabatic state). (d) Schematic of the three fragment-localized orbitals (see also Figure S2) together with the singlet CSFs that can be generated by distributing four electrons in these three orbitals.

Computational details

The non-adiabatic dynamics following photoexcitation to $S_1(\pi\pi^*)$ were modeled using AIMS with adiabatic energies, nuclear gradients and non-adiabatic couplings computed using the complete active space self-consistent field (CASSCF) implementation[40-42] in a development version of the graphical-processing-unit-accelerated TeraChem program.[43-46] Specifically, we use the empirically-corrected α-CASSCF method that was recently demonstrated to be an efficient way of modeling dynamical correlation effects in HBDI⁻ across relevant geometries.[47] We used an active space consisting of four electrons in three orbitals (the bonding, non-bonding and anti-

bonding methine bridge orbitals, see Figure S2a) with averaging over the three lowest singlet states and the 6-31G* basis set, i.e., α-SA3-CASSCF(4e,3o)/6-31G*. The three-state averaging is necessary to provide a balanced description of the photoisomerization in the anionic HBDI⁻ chromophore, permitting deactivation through both bridge torsional modes.[39] The procedure used for fitting the α-parameter and its validation against extended multistate multireference second-order perturbation theory (XMS-CASPT2[48]) is described in Section S1 of the supplementary information (SI). Geometry optimization, minimum conical intersection (MECI) searches and minimum energy pathways (MEPs) were computed using the DL-FIND[49] geometry optimization library and seam MEPs using pyGSM,[50-51] both interfaced with TeraChem. XMS-CASPT2 calculations were performed using the BAGEL program.[52-53]

The initial conditions (ICs) for the AIMS simulations were sampled from a ground-state harmonic Wigner distribution at 300 K, with normal modes and harmonic frequencies computed using MP2/cc-pVDZ.[54] To avoid artificially long C–H bonds, caused by the linearization of the methyl torsions in the harmonic approximation, three normal modes, dominated by these rotations, were excluded from the sampling. Absorption spectra were generated on the basis of 500 samples using the excitation energies and oscillator strengths computed using α(0.64)-SA3-CASSCF(4,3)/6-31G*. The stick spectra were convolved with a Gaussian line shape with a full-width at half maximum of 0.07 eV and uniformly shifted by +0.16 eV to match the experimental absorption maximum for HBDI⁻ (Figure S3). To be consistent with a previous TRPES experiment on anionic HBDI⁻ in the gas-phase,[29] 30 ICs were randomly sampled under the constraint of their vertical excitation energy being located within the spectral window of the pump pulse (2.48±0.05 eV). In the AIMS simulations, only the two lowest electronic states relevant for the photodynamics were included. Each IC was initiated on S_1 under the independent first-generation approximation,[55] i.e., they are uncoupled and run independently from the beginning, and propagated using AIMS for ~10 ps ($4 \cdot 10^5$ a.u.) or until the S_1 population dropped below 0.01. The equations of motion were integrated with an adaptive time step of 20 a.u. (~0.48 fs), which was reduced upon encounter of regions with non-adiabatic coupling. A spawning threshold of 0.005 $E_h / \hbar$ (scalar product between derivative coupling and nuclear velocity vectors at a given time step) was applied and the minimum population of a trajectory basis function (TBF) to spawn was 0.01. Errors of decay time constants were estimated with the bootstrap method,[56,57] using 1500 bootstrapping samples. TBFs

on S_0 which did not couple with other TBFs for at least 5 fs were decoupled and continued independently on S_0 until the outcome immediately following internal conversion could be assigned. Specifically, TBFs that immediately after internal conversion reached an absolute I-torsion beyond 150° were classified as photoproduct generating (*E*-isomer) while those returning to an absolute I-torsion angle below 60° were regarded as ground-state recovery (*Z*-isomer). The excess energy on the hot ground state means that continued propagation will lead to additional thermal isomerization.

To rationalize the effects of geometrical deformations, we use the three-state diabatic model proposed by Olsen and McKenzie[39] (summarized in Figure 1b-d). While earlier work has focused on the coupling between charge-transfer behavior and the bridge-torsional degrees of freedom,[30, 39] we here focus on the additional geometrical deformations required to reach the intersection seam. Approximate diabatic states are constructed by block-diagonalization[58-59] of the Hamiltonian in the basis of singlet configuration state functions (CSFs) into covalent and ionic blocks. The six singlet CSFs are generated from distributing four electrons in the three fragment-localized active-space orbitals obtained from Boys localization[60] (Figure S2b). Further details are provided in Section S2. Importantly, in this orthonormalized fragment-localized basis, bond formation is a result of mixing between a covalent configuration and its corresponding bond-polarizing ionic configurations.[61] The covalent–ionic coupling is mainly governed by resonance integrals between the relevant fragment-localized orbitals but also by the interaction with the remaining closed-shell electrons. In particular, geometrical deformations leading to a simultaneous interaction of the I- and P-ring localized orbitals (*i* and *p*, respectively) with the bridge orbital (*b*) result in a coupling between the $\left| P \right\rangle$ and $\left| I \right\rangle$ diabatic states, dominating the adiabatic S_0 and S_1 states, and hence, in turn, increases the S_1/S_0 energy gap. Vertical electron affinities of the methyl-truncated P- and I-rings were computed using SA3-XMS-CASPT2/6-31G* with active spaces (8/7e,7o) and (8/7e,6o) (anionic/neutral radical) and geometrical parameters corresponding to the S_1-P and the S_1-I minimum, respectively.

Results and discussion

A prerequisite to elucidate the importance of the two competing deactivation pathways is the ability of the level of theory used in the non-adiabatic dynamics to capture the relative energetics along the key I- and P-torsional modes. As validated by comparison to XMS-SA3-CASPT2(4,3)

results (Section S1), α(0.64)-SA3-CASSCF(4,3) correctly reproduces the energetic ordering of the S_1 twisted configurations with respect to the FC point. In particular, only the I-twisted MECI is energetically accessible from the FC point, consistent with previous high-level calculations.[35] Note that correspondingly small active-space CASSCF calculations are inadequate to capture the relative energetics of the FC point and MECIs even qualitatively (data not shown). Geometric parameters of key critical points and their relative ground- and excited-state energies at both levels of theory are provided in Figure S4 and Tables S1/3-4. As noted earlier, progress along either of the torsional modes is almost barrierless and fluorescence from the shallow planar S_1 minimum is recoverable only at low temperatures.[22] Although we find a small barrier along ϕ_P (~0.01 eV), we note that the S_1 planar structure does not represent a minimum at the α-CASSCF level of theory due to the absence of a barrier along ϕ_I (Figure S5). Nevertheless, because of the substantial total initial kinetic energy (2.79 eV, half the energy of the zero-point vibrational energy on the ground state as obtained from the Harmonic Wigner sampling) and the negligible torsional barriers, we do not expect this discrepancy to be critical for determining the branching ratio of the competing twisting pathways at the present conditions. In other words, α-CASSCF offers a sufficiently accurate and efficient route to explore dynamical effects in the excited-state deactivation of HBDI⁻.

Figure 2 presents the S_1 population decay profile for gas-phase HBDI⁻ obtained from the α-CASSCF AIMS simulations initiated from 30 initial conditions, randomly sampled from the finite-temperature (300K) harmonic Wigner distribution with the constraint of having a vertical excitation energy falling within 2.48±0.05 eV. This energy is slightly red-detuned with respect to the linear absorption maximum (see Figure S3) and mimics the pump energy used in the previous TRPES study[29] on the internal conversion dynamics. The relaxation is characterized by three different time scales: an ultrafast femtosecond component, an intermediate and a longer-lived picosecond component. Initially after photoexcitation, there is a definite lag period before any population transfer to S_0 is observed. Fitting of the S_1 population profile (based on the ~10 ps simulation) to a delayed biexponential decay yields a lag time of 177±35 fs and decay time constants of 909±169 fs and 9.0±5.1 ps with amplitudes of 83 and 17%, respectively. This indicates that most of the wavepacket undergoes fast internal conversion to the ground state while a fraction remains trapped on S_1 for longer times. These time scales agree reasonably well with the experimental time constants reported for gaseous HBDI⁻ at ambient temperature (300-330 fs, 1.3-

1.4 ps and >10-11.5 ps).[22, 29] Although a rigorous experiment–theory comparison requires calculation of the relevant experimental observable (e.g., TRPES) and remains a task for future work, this overall good agreement lends credence to the following analysis of the simulations.
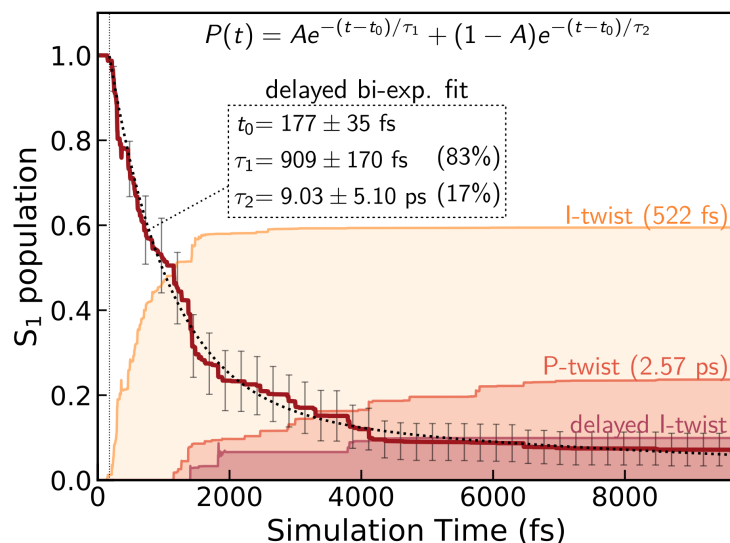

$$P(t) = Ae^{-(t-t_0)/\tau_1} + (1-A)e^{-(t-t_0)/\tau_2}$$

delayed bi-exp. fit
$t_0 = 177 \pm 35$ fs
$\tau_1 = 909 \pm 170$ fs (83%)
$\tau_2 = 9.03 \pm 5.10$ ps (17%)

I-twist (522 fs)

P-twist (2.57 ps)

delayed I-twist

Figure 2. S_1 population decay obtained from the $\alpha(0.64)$-SA3-CASSCF(4,3) AIMS dynamics together with a delayed bi-exponential fit (black dashed line). The labels give the lag time as well as the two decay time constants and their amplitudes (in parentheses). Associated error bars are standard errors estimated by bootstrapping with 1500 boot cycles. About 10% of the population remains trapped on S_1 by the end of the simulation time (~10 ps). The colored shadings indicate the decomposition of the S_0 re-population into direct I- and P-twisting pathways as well as indirect I-pathway through intermediate P-twisted geometries (see Figure 5). These were computed as the incoherent sums over TBF populations associated with S_0.

Origin of delayed bi-exponential decay.

From a theoretical perspective, most of our current understanding has been inferred from static calculations, suggesting bridge torsions and pyramidalization as key coordinates for ultrafast deactivation.[33-35] To investigate the dynamical importance of these coordinates and elucidate the mechanistic details underlying the experimentally reported time scales, we analyze the progress of the excited-state wavepacket following photoexcitation and characterize geometries at which the population transfer to the ground state occur.

Figures 3a and b display the initial ~2 ps time evolution of the one-dimensional reduced S_1 densities along the ϕ_I and ϕ_P dihedrals, respectively. The reduced densities were computed using the Monte Carlo procedure described in Ref. 62. The blue filled circles indicate spawning geometries (i.e., the centroid positions of the spawned TBFs) associated with non-adiabatic population transfer events. Departure from the FC region involves redistribution of vibrational

energy into the two bridge torsional coordinates as facilitated by a weakening of the methine bridge bonds on S_1. Owing to the asymmetry of the I-ring, oppositely directed I-twisted geometries are enantiomers, while the corresponding P-twisted structures are identical. Consistent with the essentially barrierless potential energy curve along both torsional modes, roughly half of the population (~40%) initially undergoes ϕ_P twisting while the remaining proceeds along ϕ_I. The onset of the population decay coincides with near orthogonally I-twisted configurations, and the appearance of partial wavepacket revivals (frequency of 38 ± 11 cm^{-1}, as obtained from a Fourier-component analysis of individual TBFs) is indicative of a sloped access to the conical intersection seam (only ~34% of the population is transferred during the first spawning event). Displacement along the ϕ_P mode exhibits more pronounced oscillations (frequency of 48 ± 18 cm^{-1}), and the excited-state wavepacket largely remains trapped on S_1 beyond the first ~2 ps. The higher frequency component (582 ± 54 and 611 ± 100 cm^{-1} along P- and I-twisted pathways, respectively) appearing in the reduced densities along both torsional modes originates from bridging methine hydrogen out-of-plane (HOOP) motion (see below).
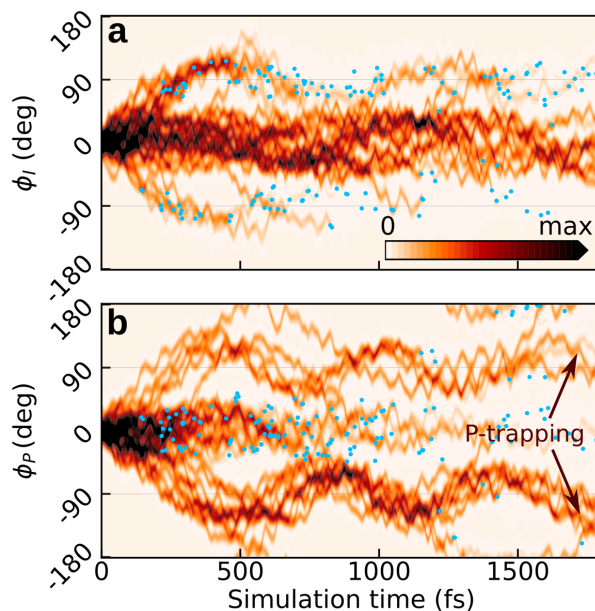

Figure 3. Time evolution of the S_1 wavepacket density along the bridge torsional modes within the first 1.8 ps after photoexcitation. S_1 reduced density projected onto the (a) ϕ_I and (b) ϕ_P dihedral angles. While motion along the ϕ_I dihedral mediates significant population transfer, the ϕ_P torsional mode leads to population trapping on S_1 for longer time scales. Blue filled circles indicate the location of non-adiabatic transition events. The slightly asymmetric density distributions with respect to the two torsional directions are likely a result of the relatively small number of initial conditions used in this work since the underlying potential energy profiles are symmetric.

The (ϕ_I, ϕ_P)-distribution of spawning geometries over the course of the simulation is shown in Figure 4c. The non-adiabatic transition events cluster into two distinct decay pathways, dominated by torsional motion along either one of the bridge dihedrals. Although these geometries largely resemble the two types of MECIs reported previously,[33, 63-65] here labeled MECI-I$^{+/-}$ and MECI-P$^{+/-}$ according to rotation direction (Figures 4a-b/S6 and Table S4), the sloped access to the intersection seam combined with the significant nuclear kinetic energy gained upon twisting means that higher-energy regions of the seam become increasingly relevant in the dynamics. This is seen from the distribution of S_1/S_0 energy gaps and the energetic locations of the spawning geometries relative to the geometrically nearest MECI (Figures 4d-e). As shown by decomposing the re-population of S_0 according to torsional mechanism (filled curves in Figure 2), the I-twisting pathway accounts for the majority of the population transfer (~60% via direct decay, see below) while only ~20% transfers at P-twisted geometries. The remaining population (~20%) is equally split between P-trapping on S_1 and delayed internal conversion via the I-twist pathway following temporary trapping along ϕ_P. In the latter case, the initially P-twisted subpopulation is reflected back via the planar configuration to reverse the charge-transfer direction rather than following a higher-energy hula-twist like motion,[66] i.e., concerted rotation around both bridge bonds.

The delayed onset and less efficient decay through the P-twist pathway is consistent with MECI-P$^{+/-}$ being energetically inaccessible from the FC point (see Figure S4). In addition to the diabatic state-selective stabilization mediated by an asymmetric bond stretching across the bridge (preferentially stabilizing either the phenolate or quinoid resonance structure), access to the minima on the intersection seams requires pyramidalization of the methine C atom. The gradient difference vectors at both types of MECIs are dominated by this collective pyramidalization and bond-stretch motion whereas the derivative coupling vectors mainly represent the torsional motion around the respective bridge bond (Figure S7). Consistent with the dynamical behavior discussed above, both types of MECIs are sloped and following the associated paths of steepest descent on S_0 leads to recovery of the original Z-isomer (data not shown). The pyramidalization on S_1 is governed by the faster methine HOOP motion, which primarily gains amplitude upon twisting, and its direction is initially dictated by that of the activated torsional mode (Figure S8). The stronger electron affinity of the P-ring (vertical electron affinities of 1.24 and 0.64 eV for the P- and I-ring, respectively) leads to a larger S_1/S_0 energy gap at P-twisted geometries (Figure 1a, Table S1).[35] Within the three-state diabatic model, this asymmetry is a result of comparatively

larger contributions from stabilizing ionic configurations to the diabatic $\left|P\right\rangle$ state at P-twisted geometries compared to the corresponding ionic contributions to the $\left|I\right\rangle$ state at I-twisted geometries (Figure S9b). Thus, pyramidalization acts as a diabatic-state biasing potential that preferentially destabilizes the torsionally-decoupled diabatic state by reducing the contributions from ionic configurations, thereby closing the energy gap. For this reason, a higher degree of pyramidalization is needed to access the P-twisted intersection seam.
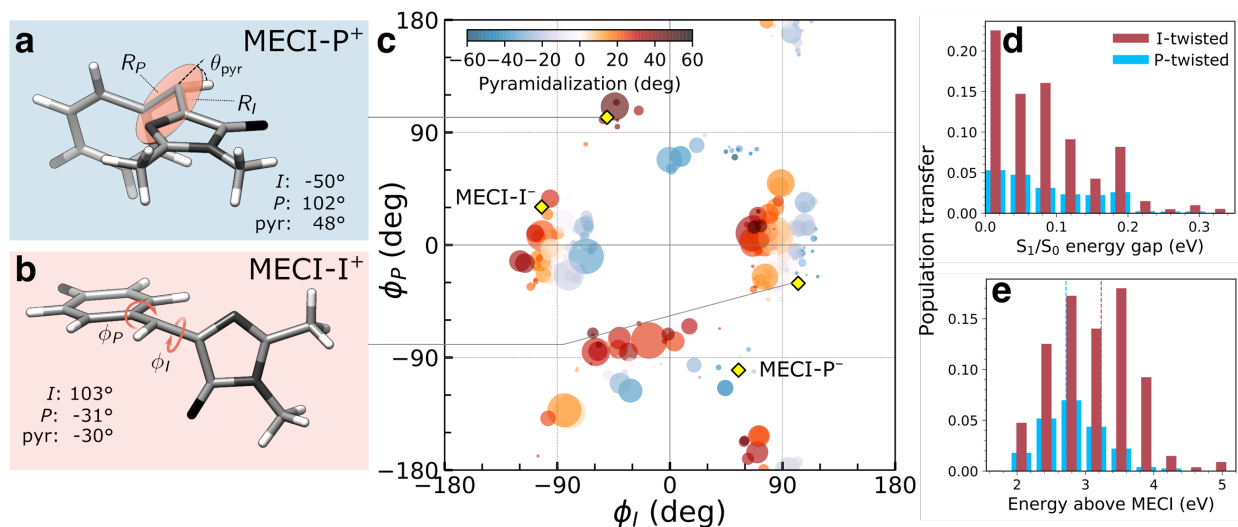

Figure 4. Geometric characterization of non-adiabatic transition events. Structures of (a) MECI-I$^+$ and (b) MECI-P$^+$ highlighting key geometric parameters (definitions are given in Figure S1). (c) Distribution of (ϕ_I, ϕ_P)-dihedrals at the spawning geometries. The size and color of each circle represent absolute population transfer and extent of bridge pyramidalization, respectively. The absolute population transfer is defined as the total population gained by the child TBF from the beginning of the coupled propagation until the gain drops below a threshold value of 10^{-4}. Efficient population transfer is associated with significant pyramidalization of the methine bridge. Yellow diamonds indicate the location of MECIs. (d) Absolute population transfer versus S_1/S_0 energy gap at the non-adiabatic transition events divided according to the decay pathway. (e) Distribution of the S_1 energies at the I- and P-twisted spawning events relative to the geometrically closest MECI. The vertical dashed red (blue) line corresponds to the sum of the zero-point kinetic energy in the ground-state (within a harmonic approximation) and the energy gap between the FC point and MECI-I$^+$ (MECI-P$^+$) geometry.

Upon reaching the electronic ground state, the absence of channels for intermolecular energy dissipation will over longer time scales lead to chemical transformations of the vibrationally hot HBDI$^-$, including fragmentation and electron emission. However, whether the preceding internal conversion process directly produces E-isomer via photoisomerization remains an open question. To investigate this, we followed the dynamics on S_0 until the outcome of internal conversion could be assigned. Specifically, we classified TBFs reaching an absolute ϕ_I of 150° immediately following population transfer as successful photoisomerization while those returning to angles

below 60° counted as recovery of the original *Z*-isomer. The similar criterion for ϕ_P was used to identify P-flipped configurations. While 59% of the excited-state decay leads to recovery of the ground state (of which 14% also undergoes indistinguishable P-flip), a notable 41% generates photoproduct. Considering only the I-twisted decay, the photoisomerization quantum yield increases to ~50%.

The main features of the excited-state decay mechanisms in isolated HBDI⁻ appearing from our simulations are provided in Figure 5. The lifetimes and yields of each key process are highlighted. Photoexcitation is followed by bifurcation of the wavepacket in near-equal proportions along the two alternative bridge torsional coordinates. The ~180 fs lag time corresponds to the time associated with vibrational energy redistribution from FC-active vibrations (low-frequency bridge-bending and high-frequency bridge-stretching modes[35, 67]) into the torsional modes required to reach the intersection seams. Not surprisingly, based on the shorter plateau and steeper torsional gradient with α-CASSCF compared to XMS-CASPT2 (Figure S5), this delay time is shorter than the reported experimental values of ~300 fs. The ~1 ps component of the bi-exponential decay is dominated by the faster excited-state relaxation through the I-torsional pathway (~0.5 ps) with a smaller but slower contribution from P-torsional mediated decay (~2.6 ps). This was confirmed by fitting the S_1 population decay using the lag and rise times derived from the associated re-population curves in Figure 2. The longer time-scale component is a consequence of a fraction being trapped on S_1 along the P-torsional mode. We note that the extent of non-adiabatic population transfer via the P-channel may be somewhat overestimated given the energetic closer proximity of MECI-P$^{+/-}$ to the FC point at the present level of theory (Figure S4). Nevertheless, the mechanistic insight predicted by our simulations largely supports the models previously proposed on the basis of experimental data and high-level static calculations.[35] Our dynamics results demonstrate that, indeed, internal conversion through the I-twisted intersection seam mediates photoisomerization. This is in contrast to the unreactive behavior predicted by the (artificial) S_0 minimum energy pathways starting near the MECIs. Clearly, a dynamical mapping of the intersection seam is necessary to understand the intrinsic photoisomerization propensity of HBDI⁻.
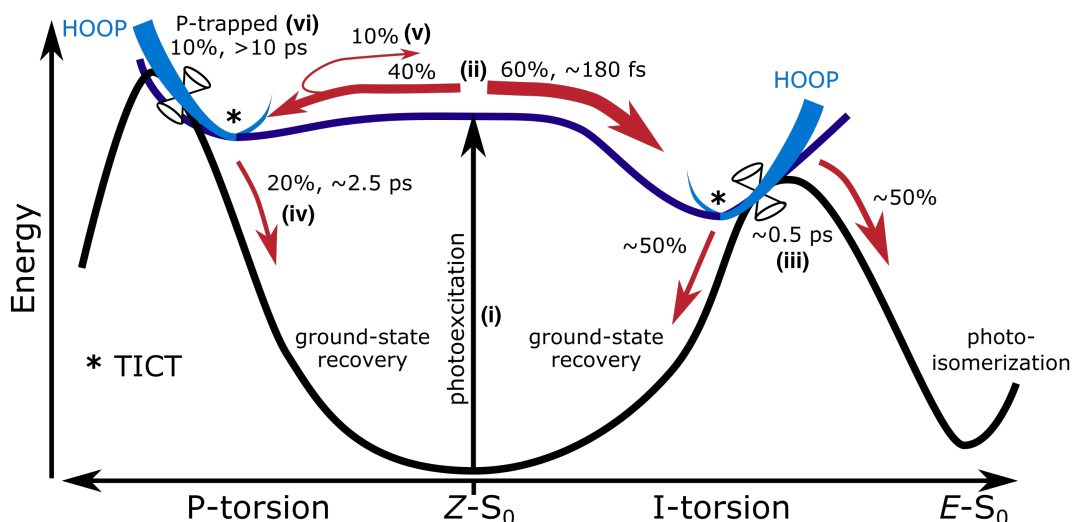
Figure 5. Schematic of the excited-state dynamics of HBDI⁻, showing (i) photoexcitation, (ii) departure from the FC point along the torsional modes, internal conversion via the (iii) I-twist, (iv) P-twist and (v) delayed I-twist pathways and (vi) trapping along the P-channel. Branching ratios and time scales from the AIMS dynamics indicated.

Mapping the sloped I-twisted intersection seam.

To this end, we consider the dynamically accessed regions of the I-twisted intersection seam, focusing on the positive I-twist direction (MECI-I⁺). Figure 6a shows the distribution and outcome of the non-adiabatic transition events along the I-torsion and HOOP coordinates, roughly approximating the branching space in a first-order analysis, together with contour plots of the S_0 and S_1 potential energy surfaces (PESs). The corresponding three-dimensional representations of the PESs are shown in Figure 5b. The torsional axis was obtained from a relaxed scan along the I-torsion with the P-torsion constrained at 0°, and therefore, it also includes adjustments of bond distances and angles. The HOOP axis was obtained from a subsequent unrelaxed scan, starting from the relaxed structures.

The non-adiabatic population transfer events (shown as markers) tend to follow a bimodal distribution with maxima centered around "out-of-phase" configurations (see also Figure S6). These are defined as geometries where the pyramidalization direction of the methine C atom is opposite of the sign of the torsional displacement relative to a 90° I-twist (Figure 6c). At these geometries, simultaneous pyramidalization and a near-orthogonal arrangement of the localized i and b orbitals are achieved. This preserves the approximate block-diagonal structure of the Hamiltonian (i.e., a two-dimensional $|P\rangle$ and $|B\rangle$ (S_1/S_2) block and a one-dimensional $|I\rangle$ block for S_0), characteristic of the I-twisted S_1 minimum (Figure 1b) and leads to a concomitant

preferential destabilization of the diabatic $|I\rangle$ state, as required to reach the S_1/S_0 degeneracy (see Figure 6d and diabatic state composition in Figure S9 and Table S6). Ignoring the small asymmetry arising from the weak electronic coupling of the p and b orbitals with the i orbital at I-twisted configurations, we may expect two MECIs related by a mirror plane perpendicular to the I-ring and passing through the I-bond. Indeed, in addition to MECI-I$^+$, we located an essentially isoenergetic MECI, labeled MECI-I2$^+$. While the population transfer efficiency is similar for both MECIs, the region around MECI-I2$^+$ is reached earlier in the dynamics due to its closer proximity to the FC point. Consequently, the majority of the I-twisted population transfer (64%) occurs in the vicinity of MECI-I2$^+$. The seam MEP connecting the two MECIs is characterized by a small barrier of ~0.1 eV, associated with planarization of the methine C-atom and a ~0.03 Å lengthening of the C_5–C_6 bond (see gray line connecting the yellow markers in Figure 6b and Figure S8a). The topography along the seam MEP remains sloped towards the photoreactant (see Figure S8b). We note that the direction and degree of the P-torsion at both MECIs are governed by the pyramidalization so as to maximize the alignment of the p orbital and the now increasingly sp^3-hybridized b orbital. However, motion along ϕ_P is associated with only a small energy-gap penalty (i.e., it is outside the branching space within the first-order approximation) easily compensated by small bond and angle changes. Therefore, population transfer occurs over an extended region of the seam where the P-ring can be misaligned with respect to the bridge pyramidalization. In particular, in the $(\phi_I, \phi_P)=(+90°,>0°)$ quadrant (see Figure 4c), the topography becomes sloped towards the photoproduct (Figure S10). In the following, we disregard such displacement along ϕ_P in the geometric classification of the non-adiabatic events.

In contrast to the non-productive picture provided by the seam MEP analysis, the dynamics suggests a correlation between the location of the non-adiabatic population transfer events and the outcome of the internal conversion: The ratios between reactive and unreactive outcome of the internal conversion at the MECI-I$^+$ and MECI-I2$^+$ (combining data for both positive and negative ϕ_I-values) are ~3:1 and ~1:2, respectively. However, it should be noted that the combination of the earlier encounter of MECI-I2$^+$ means that the photochemical production of the E-stereoisomer is approximately equally distributed around both MECIs. But where does this difference in photoreactivity around the two MECIs come from?
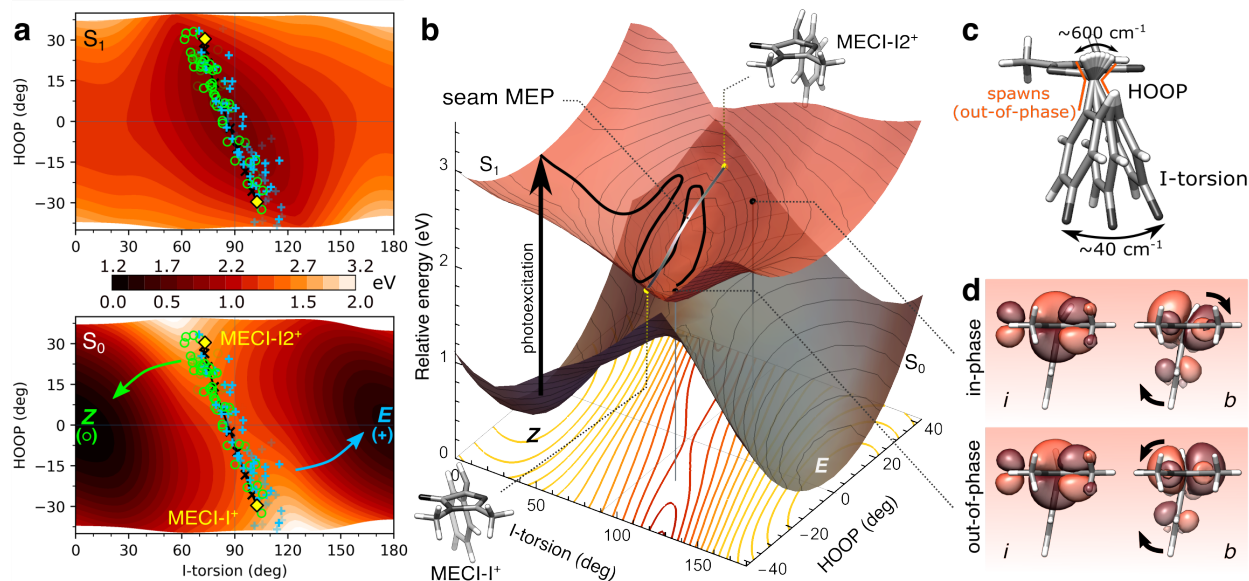
Figure 6. The implications of HOOP on photoproduct generation along the positive I-twist mediated decay pathway. (a) Contour plots of the S_1 (top) and S_0 (bottom) PESs along the I-torsion and HOOP modes. These have been obtained by a fixed HOOP scan along a scan of the I-torsion keeping the P-torsion fixed at zero, while all remaining coordinates were allowed to relax. MECIs are highlighted by the yellow diamonds while non-adiabatic transitions leading to ground-state recovery (*Z*-isomer) are indicated by open green circles and those producing photoproduct (*E*-isomer) by blue crosses. These roughly correspond to each peak in the approximate bimodal distribution (see Figure S6). The black line shows the seam MEP connecting MECI-I$^+$ and MECI-I2$^+$ (see gray line in (b) and Figure S8). The MECIs are reached by tuning the bond distances (in particular, the P-bond and C_5–C_6 are extended by ~3 and 4 pm, respectively) and contraction of the bridge angle by ~6.8°. The main effect of this is a destabilization of S_0 (not shown) and a rotation of the S_0 ridge. (b) Three-dimensional representation of the PESs in (a). The contour plot below shows the energy gap between the S_1 and S_0 states, indicating a smaller gap (red) at out-of-phase geometries. The MECIs are shown as yellow points, and the seam MEP as the connecting gray line. The two black points on the S_1 surface correspond to out-of-phase and in-phase configurations at the same I-torsion angle, see (d). (c) Schematic representation of the HOOP and I-torsional modes with estimates of their frequencies as obtained from the dynamics. As indicated in (a), population transfer occurs when the two modes are out-of-phase. (d) Boys-localized orbitals on the I-ring and the methine bridge (labeled *i* and *b*, respectively) for the in-phase and out-of-phase configurations indicated in (b). Isovalue: 0.03 a.u. The HOOP direction at out-of-phase configurations counteracts the rotation of the *b*-orbital relative to the *i*-orbital induced by the I-torsion, thereby maintaining an effectively orthogonal arrangement of these orbitals similar to the situation at the 90° I-twisted minimum (S_1-I, Figures 1a/b).

Origin of different dynamical behaviors.

To uncover the origin of the difference in photoreactivity between the two I-twisted MECIs, we investigated the implications of inertial effects, i.e., the velocity and direction of the approach to and exit out of the different regions of the I-twisted intersection seam. While inertial effects through the interplay between effective coupling strength and interaction time dictate the efficiency of population transfer,[68-69] we here focus on how they affect the outcome of the internal

conversion process. Two limiting regimes can be envisioned. In the first limit, the nonadiabatic transitions occur at classical turning points within the branching space, i.e., at velocities with comparatively small components along the g- and h-vectors, such that the outcome is dictated by the momentum gained on the ground state. In the second regime, the population transfer occurs with substantial kinetic energy in the branching space. To explore these limits, we considered the photoproduct distributions obtained from ground-state dynamics starting from cone sampling (i.e., geometric displacement within the branching space of the two MECI-Is) and the following two constructed sets of initial velocities: (i) zero initial velocities, where the only source of kinetic energy comes from the acceleration induced by the ground-state PES, and (ii) starting with all kinetic energy (~0.44 eV, corresponding to the energy difference between the FC point and the MECI-I$^+$) initially associated with the branching space. To investigate the dynamical photoreactivity, we further estimate the committor distribution[70-71] around each of the two MECI-Is. Specifically, we considered the outcome of randomly sampling the atomic velocities from a Gaussian distribution with subsequent mass-weighting and uniform scaling to yield an initial kinetic energy equal to the sum of the kinetic energy of the ground state (within the harmonic approximation) and the energy gap between the FC point and MECI-I$^+$ (~0.44 eV). With the exception of configurational sampling around rather than at the MECIs, our procedure follows that in the Appendix of Ref. [72] with 50 samples of randomized initial velocities per configuration. This gives an estimate of the probability of generating photoproduct under the assumption of a thermalized state, as characterized by equipartitioning of the kinetic energy. Although thermalization is not expected during the ultrafast internal conversion, this analysis nevertheless provides insight into the influence of having non-zero kinetic energy within the intersection space.

Figures 7a-b summarizes the results for the zero- and random-initial-velocity sampling schemes applied to the two MECI-Is whereas those obtained from non-zero velocities restricted to the branching space are shown in Figure S11. The location of each point in the polar plots represents the geometric displacement within the branching plane while its color indicates the outcome of the ground-state dynamics or the probability of photoproduct formation for the zero- and random-initial-velocity sampling schemes, respectively. In the latter case, the committor for each displacement is computed as the fraction of samples that reach the E-isomer prior to undergoing thermal isomerization on S_0 back to the Z-isomer. At low velocities in the branching plane, the location of the non-adiabatic population transfer on the I-twisted intersection seam

determines the outcome, and photoproduct formation is confined to regions corresponding to displacements in the +h-direction and only around MECI-I$^+$. At higher velocities restricted to the branching space, the dissimilarity between the two MECI-Is largely disappears (Figure S11), and the exit direction within the branching space now decides which product will be formed. In particular, the h-vector represents the isomerization-driving coordinate, and velocity along this direction promotes photoproduct generation irrespective of the location of the non-adiabatic transition (MECI-I$^+$ or MECI-I2$^+$). A similar imprint of the +h-direction (in terms of both displacement and exit direction) is obtained upon introducing initial kinetic energy in the remaining degrees of freedom. The black line represents the geometries at which initiating ground-state dynamics will lead to ground-state recovery and photoproduct generation with equal probability. Consistent with the dynamics, we recover the picture of MECI-I$^+$ being more photoreactive than MECI-I2$^+$, and the comparison between the three different sets of initial conditions suggests that this intrinsic difference originates from the asymmetry of the I-ring as will be discussed next.

The different dynamical behaviors around the MECI-Is at zero initial velocities can be explained by the directional bias of the momentum gained along the lighter HOOP coordinate upon reaching the ground state. The direction of steepest descent governing the early dynamics on S_0 involves a shortening of the C_5–C_6 bond (see schematic in Figure 7a and the gradient difference vector in Figure S6). This results in a fast, asymmetric contraction of the I-ring that, in turn, induces oppositely directed HOOP motion for the two MECI-Is before any significant displacement of the slower I-torsional mode takes place. For MECI-I$^+$, this promotes crossing of the S_0 ridge thereby enabling photoproduct generation, while impeding it for MECI-I2$^+$ (see Figure 7a). To test this interpretation, we artificially increased the mass of the methine H-atom to that of a methyl group (~15 amu). We note that a recent study by Conyard *et al.* investigated the effect of bridge methylation and found accelerated non-radiative decay.[73] However, the resulting steric crowding introduces non-negligible of potential effects. On the other hand, introducing a fictitious heavier hydrogen allows us to investigate purely inertial effects by specifically lowering the momentum gain along the HOOP coordinate on S_0 and diminishing the effective mass difference between the HOOP and torsional degrees of freedom. At zero initial velocities motion along the heavier HOOP mode is no longer fast enough to mediate barrier crossing prior to activation of the torsional mode, thereby preventing photoproduct generation around MECI-I$^+$ (Figure S12).

The central question then becomes what characterizes the dynamical behavior of the system? In other words, what is actual velocity distribution upon reaching the intersection seam? As expected from the oscillatory behavior along ϕ_I, the overall distribution of velocity components along the h-vector at the non-adiabatic transition events is symmetric and similar for both MECI-Is (Figure S13a). About 70% of the I-twisted population transfer occurs with a kinetic energy contribution along the h-direction that is larger than the kinetic energy per degree of freedom assuming equipartitioning among all vibrational degrees of freedom. Moreover, as indicated in Figure 6a, a separation based on the outcome of the internal conversion process reveals a correlation between the direction of the component along the h-vector and the photoproduct: ground-state recovery close to MECI-I$^+$ is associated with a positive velocity component whereas photoproduct formation in proximity to MECI-I2$^+$ is mostly associated with a negative velocity component. An opposite but much weaker trend is observed for the reverse cases. The corresponding picture weighted by the absolute population transfer is provided in Figure S13b. Together, these results show that the ~50% photoisomerization quantum yield for the I-twisted population is a consequence of two effects: (i) the initial approach to the MECI-I2$^+$ region of the seam where non-statistical conditions prevail and there is significant velocity along the isomerization-driving +h-direction (i.e., driven by inertial effects on S_1), and (ii) the intrinsic higher photoreactivity of MECI-I$^+$ compared to MECI-I2$^+$ (i.e., mostly governed by the photoproduct-favoring inertial effects gained on the ground state caused by the asymmetry of the I-ring).

Our analysis suggests a possible strategy for optimizing the rate and quantum yield of photoisomerization of HBDI$^-$. We recall that the appearance of the out-of-phase MECI-Is is a consequence of the non-vanishing S_1/S_0 energy gap at I-twisted structures: it necessitates vibrational redistribution from the isomerization-driving I-torsion into the HOOP coordinate to reach the intersection seam. Applying a diabatic biasing potential, such as through a chemical modification or mutations of the protein scaffold, to selectively destabilize the torsionally-decoupled $\left| I \right\rangle$ state, could potentially remove the need for pyramidal motion, thereby changing the double-well on the seam to a single well with its minimum located near or coinciding with the I-twisted minimum. This could potentially lead to a more direct approach to the intersection seam along the isomerizing-driving I-torsional coordinate with a consequent increase in rate and yield of photoisomerization. The extent to which such strategy would be transferable to the chromophore

inside a protein remains to be investigated given that particular movement may be arrested in the protein. Most apparently, conformational restrictions may direct the wavepacket towards alternative regions of the intersection seams, dynamically inaccessible in the gas phase, and not considered in this work. Indeed, the volume-conserving high-energy hula-twist motion in the isolated chromophore has been suggested as deactivation pathway in several GFP relatives.[74-76]
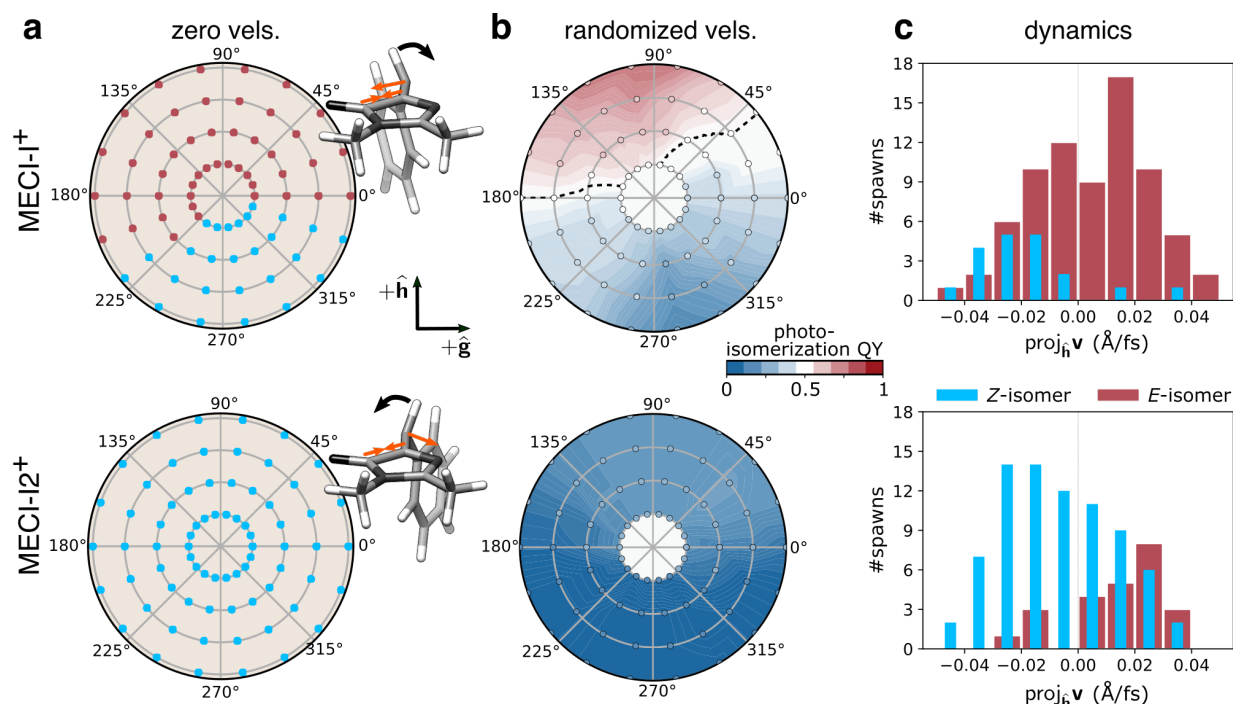

Figure 7. Implications of inertial effects on photoproduct generation from the I-twisted intersection seam. Top panel: MECI-I$^+$; bottom panel: MECI-I2$^+$. Photoproduct distribution at each displacement within the branching plane, as given by the polar coordinates (radii: 0.005-0.02 a.u. in steps of 0.005 a.u.), based on the outcome of dynamics starting from (a) zero initial velocities. The asymmetric contraction of the I-ring and methine planarization on S$_0$ (orange arrows) lead to oppositely directed acceleration of the HOOP motion (black arrows) for the two MECI-Is. This promotes photoproduct formation at MECI-I$^+$ while inhibiting at MECI-I2$^+$; (b) 50 initial conditions with randomized velocities. The black line represents the isocommittor line corresponding to 50% photoproduct generation. (c) Distributions of the velocity components for the parent TBF along the h-direction at the non-adiabatic transition events close to the two types MECI-Is and categorized based on the outcome of the ensuing S$_0$ dynamics. Events for both positive and negative ϕ_I directions have been combined. In line with the photoproduct distributions in (b), photoisomerization near MECI-I2$^+$ correlates with a positive component along the h-direction, and ground-state recovery from MECI-I$^+$ with a negative component.

Conclusions

In summary, we have simulated the excited-state dynamics of the isolated HBDI⁻ chromophore following photoexcitation to $S_1(\pi\pi^*)$. Our simulations are in good agreement with experimental time scales enabling us to provide mechanistic insight into the intrinsic photoresponse of the chromophore. Our findings can be summarized as follows. The excited-state population predominantly undergoes ultrafast internal conversion through the I-twist pathway with only a minor fraction (~10%) decaying through the competing P-twist pathway. However, the combination of equitable initial branching along the two pathways and existence of a P-twisted minimum on S_1 leads to P-trapping on longer timescales. The near mirror symmetry of the bridge-pyramidalized and I-twisted geometries introduces two minima on the I-twisted intersection seam (MECI-I⁺ and MECI-I2⁺) that dynamically display opposite trends in terms of photoproduct formation. By mapping the photoreactivity of each of the MECI-Is via a committor analysis and studying the influence of the exit direction on the outcome of the internal conversion process, we identified the origin of this difference: the asymmetry of the I-ring leads, upon reaching the ground state, to differently directed momenta towards bridge planarization, promoting selectively either photoproduct generation (MECI-I⁺) or ground-state recovery (MECI-I2⁺). Despite its lower photoreactivity, the earlier encounter of MECI-I2⁺ during the dynamics combined with the initial vibrational energy redistribution into the isomerization-driving I-torsional mode implies that internal conversion near both minima on the seam contribute about equally to photoproduct formation. In other words, our work suggests that the experimentally evidenced photo-induced production of *E*-isomer[27] not only originates from thermal isomerization on the vibrationally hot ground state but also from direct passage through the I-twisted intersection seam.

The present explanatory study lays the foundation for future work focused on manipulation: specifically, addressing the extent to which perturbative effects, be it inertial or potential (steric/electronic), induced by substituents or environmental modifications can be introduced to tailor the outcome of photoexcitation of the HBDI⁻ chromophore. Tuning the photoisomerization quantum yield is important not only in the traditional imaging role through super-resolution microscopy[8-9, 77] but also for emerging opportunities within optogenetics. For example, light-activated strand-dissociation of split-GFP constructs could be used as an optogenetic tool for protein control but their utility is currently limited by the low yield of the strand-exchange-inducing photoisomerization.[78-79] Two key focus areas for such photoswitching

applications are: (i) Biasing the early dynamics towards the reactive I-twist channel. The non-selectivity of the torsional pathways upon departure of the FC point inherent to the isolated chromophore, leading to almost equal bifurcation of the wavepacket into the I- and P-channels. (ii) The rate and efficiency of photoisomerization along the reactive I-twist pathway. Although a strict distinction between effects of the surrounding protein and direct chromophore modifications cannot be made, the recent time-resolved fluorescence study on Dronpa2 variants by Romei *et al.* indicates the potential of using chemical substitution on the P-ring to selectively modify the excited-state torsional barrier by tuning the electronegativity of the substituent and hence the route taken by the excited-state wavepacket. As for point (ii), the fact that internal conversion is gated by the HOOP motion in HBDI$^-$ hints that a potential of modifying the approach towards the intersection seam by shifting the location of the MECI towards being the minimum on the S_1 PES. Ideally, this would translate into higher kinetic energy in the isomerization-driving I-torsional coordinate with a consequent accelerated internal conversion and increased photoisomerization quantum yield. Work is currently underway to explore these possibilities.

Acknowledgments

Supplementary Information

Validation of α-CASSCF against XMS-CASPT2, relative energies at critical point geometries, analysis of the intersection parameters for the I- and P-twisted MECIs, three-state diabatic-state analysis, critical point geometries are provided in the supplementary information.

References

1.   Ormö, M.; Cubitt, A. B.; Kallio, K.; Gross, L. A.; Tsien, R. Y.; Remington, S. J. Crystal Structure of the Aequorea victoria Green Fluorescent Protein. *Science* **1996,** *273* (5280), 1392-1395.

2.   Shimomura, O.; Johnson, F. H.; Saiga, Y. Extraction, Purification and Properties of Aequorin, a Bioluminescent Protein from the Luminous Hydromedusan, Aequorea. *Journal of Cellular and Comparative Physiology* **1962,** *59* (3), 223-239.

3.   Shimomura, O. Structure of the chromophore of Aequorea green fluorescent protein. *FEBS Letters* **1979,** *104* (2), 220-222.

4.   Prasher, D. C.; Eckenrode, V. K.; Ward, W. W.; Prendergast, F. G.; Cormier, M. J. Primary structure of the Aequorea victoria green-fluorescent protein. *Gene* **1992,** *111* (2), 229-233.

5.   Giepmans, B. N. G.; Adams, S. R.; Ellisman, M. H.; Tsien, R. Y. The Fluorescent Toolbox for Assessing Protein Location and Function. *Science* **2006,** *312* (5771), 217-224.

6.   Rodriguez, E. A.; Campbell, R. E.; Lin, J. Y.; Lin, M. Z.; Miyawaki, A.; Palmer, A. E.; Shu, X.; Zhang, J.; Tsien, R. Y. The Growing and Glowing Toolbox of Fluorescent and Photoactive Proteins. *Trends Biochem Sci* **2017,** *42* (2), 111-129.

7.   Tsien, R. Y. The green fluorescent protein. *Annu Rev Biochem* **1998,** *67*, 509-44.

8.   Hofmann, M.; Eggeling, C.; Jakobs, S.; Hell, S. W. Breaking the diffraction barrier in fluorescence microscopy at low light intensities by using reversibly photoswitchable proteins. *Proceedings of the National Academy of Sciences of the United States of America* **2005,** *102* (49), 17565-17569.

9.   Dickson, R. M.; Cubitt, A. B.; Tsien, R. Y.; Moerner, W. E. On/off blinking and switching behaviour of single molecules of green fluorescent protein. *Nature* **1997,** *388* (6640), 355-358.

10.   Andresen, M.; Stiel, A. C.; Fölling, J.; Wenzel, D.; Schönle, A.; Egner, A.; Eggeling, C.; Hell, S. W.; Jakobs, S. Photoswitchable fluorescent proteins enable monochromatic multilabel imaging and dual color fluorescence nanoscopy. *Nature Biotechnology* **2008,** *26* (9), 1035-1040.

11.   Grotjohann, T.; Testa, I.; Leutenegger, M.; Bock, H.; Urban, N. T.; Lavoie-Cardinal, F.; Willig, K. I.; Eggeling, C.; Jakobs, S.; Hell, S. W. Diffraction-unlimited all-optical imaging and writing with a photochromic GFP. *Nature* **2011,** *478* (7368), 204-208.

12.   Acharya, A.; Bogdanov, A. M.; Grigorenko, B. L.; Bravaya, K. B.; Nemukhin, A. V.; Lukyanov, K. A.; Krylov, A. I. Photoinduced Chemistry in Fluorescent Proteins: Curse or Blessing? *Chemical Reviews* **2017,** *117* (2), 758-795.

13.   Sample, V.; Newman, R. H.; Zhang, J. The structure and function of fluorescent proteins. *Chemical Society Reviews* **2009,** *38* (10), 2852-2864.

14.   Pakhomov, A. A.; Martynov, V. I. GFP Family: Structural Insights into Spectral Tuning. *Chemistry & Biology* **2008,** *15* (8), 755-764.

15.   Day, R. N.; Davidson, M. W. The fluorescent protein palette: tools for cellular imaging. *Chemical Society Reviews* **2009,** *38* (10), 2887-2921.

16.   Lin, C.-Y.; Romei, M. G.; Oltrogge, L. M.; Mathews, I. I.; Boxer, S. G. Unified Model for Photophysical and Electro-Optical Properties of Green Fluorescent Proteins. *Journal of the American Chemical Society* **2019,** *141* (38), 15250-15265.

17.   Sarkisyan, K. S.; Bolotin, D. A.; Meer, M. V.; Usmanova, D. R.; Mishin, A. S.; Sharonov, G. V.; Ivankov, D. N.; Bozhanova, N. G.; Baranov, M. S.; Soylemez, O.; Bogatyreva, N. S.; Vlasov, P. K.; Egorov, E. S.; Logacheva, M. D.; Kondrashov, A. S.; Chudakov, D. M.; Putintseva, E. V.; Mamedov, I. Z.; Tawfik, D. S.; Lukyanov, K. A.; Kondrashov, F. A. Local fitness landscape of the green fluorescent protein. *Nature* **2016,** *533* (7603), 397-401.

18.   Kojima, S.; Hirano, T.; Niwa, H.; Ohashi, M.; Inouye, S.; Tsuji, F. I. Mechanism of the redox reaction of the Aequorea green fluorescent protein (GFP). *Tetrahedron Letters* **1997,** *38* (16), 2875-2878.

19.   Niwa, H.; Inouye, S.; Hirano, T.; Matsuno, T.; Kojima, S.; Kubota, M.; Ohashi, M.; Tsuji, F. I. Chemical nature of the light emitter of the Aequorea green fluorescent protein. *Proceedings of the National Academy of Sciences* **1996,** *93* (24), 13617.

20.   Litvinenko, K. L.; Webber, N. M.; Meech, S. R. Internal Conversion in the Chromophore of the Green Fluorescent Protein: Temperature Dependence and Isoviscosity Analysis. *The Journal of Physical Chemistry A* **2003,** *107* (15), 2616-2623.

21.   Kummer, A. D.; Kompa, C.; Niwa, H.; Hirano, T.; Kojima, S.; Michel-Beyerle, M. E. Viscosity-Dependent Fluorescence Decay of the GFP Chromophore in Solution Due to Fast Internal Conversion. *The Journal of Physical Chemistry B* **2002,** *106* (30), 7554-7559.

22.   Svendsen, A.; Kiefer, H. V.; Pedersen, H. B.; Bochenkova, A. V.; Andersen, L. H. Origin of the Intrinsic Fluorescence of the Green Fluorescent Protein. *J Am Chem Soc* **2017,** *139* (25), 8766-8771.

23.   Forbes, M. W.; Jockusch, R. A. Deactivation pathways of an isolated green fluorescent protein model chromophore studied by electronic action spectroscopy. *Journal of the American Chemical Society* **2009,** *131* (47), 17038-17039.

24.   Toker, Y.; Rahbek, D. B.; Klærke, B.; Bochenkova, A.; Andersen, L. H. Direct and indirect electron emission from the green fluorescent protein chromophore. *Physical review letters* **2012,** *109* (12), 128101.

25.   Horke, D. A.; Verlet, J. R. Photoelectron spectroscopy of the model GFP chromophore anion. *Physical chemistry chemical physics* **2012,** *14* (24), 8511-8515.

26.   Mooney, C. R. S.; Sanz, M. E.; McKay, A. R.; Fitzmaurice, R. J.; Aliev, A. E.; Caddick, S.; Fielding, H. H. Photodetachment Spectra of Deprotonated Fluorescent Protein Chromophore Anions. *The Journal of Physical Chemistry A* **2012,** *116* (30), 7943-7949.

27.   Carrascosa, E.; Bull, J. N.; Scholz, M. S.; Coughlan, N. J. A.; Olsen, S.; Wille, U.; Bieske, E. J. Reversible Photoisomerization of the Isolated Green Fluorescent Protein Chromophore. *J Phys Chem Lett* **2018,** *9* (10), 2647-2651.

28.   West, C. W.; Hudson, A. S.; Cobb, S. L.; Verlet, J. R. Communication: Autodetachment versus internal conversion from the S1 state of the isolated GFP chromophore anion. AIP: 2013.

29.   Mooney, C. R. S. H. D. A. C., A. S.; Simplerier, A.; Fielding, H. H.; Verlet, J. R. R. Taking the green fluorescence out of the protein: dynamics of the isolated GFP chromophore anion. *Chemical Science* **2013,** *4*, 921.

30.   Olsen, S.; McKenzie, R. H. Conical Intersections, charge localization, and photoisomerization pathway selection in a minimal model of a degenerate monomethine dye. *The Journal of Chemical Physics* **2009,** *131* (23), 234306.

31.   Dekhtyar, M.; Rettig, W.; Rozenbaum, V. Origin of states connected with twisted intramolecular charge shift in polymethine cations: a simple analytical treatment. *Journal of Photochemistry and Photobiology A: Chemistry* **1999,** *120* (2), 75-83.

32.   Olsen, S.; McKenzie, R. H. A two-state model of twisted intramolecular charge-transfer in monomethine dyes. *The Journal of Chemical Physics* **2012,** *137* (16), 164319.

33.   Martin, M. E.; Negri, F.; Olivucci, M. J. J. o. t. A. C. S. Origin, nature, and fate of the fluorescent state of the green fluorescent protein chromophore at the CASPT2//CASSCF resolution**2004,** *126* (17), 5452-5464.

34.   Olsen, S.; Lamothe, K.; Martínez, T. J. J. J. o. t. A. C. S. Protonic gating of excited-state twisting and charge localization in GFP chromophores: a mechanistic hypothesis for reversible photoswitching **2010,** *132* (4), 1192-1193.

35.   Bochenkova, A. V.; Andersen, L. H. Ultrafast dual photoresponse of isolated biological chromophores: link to the photoinduced mode-specific non-adiabatic dynamics in proteins. *Faraday discussions* **2013,** *163*, 297-319.

36.   Ben-Nun, M.; Quenneville, J.; Martinez, T. J. Ab initio multiple spawning: Photochemistry from first principles quantum molecular dynamics. *J. Phys. Chem. A* **2000,** *104* (22), 5161-5175.

37.   Curchod, B. F.; Martínez, T. J. Ab initio nonadiabatic quantum molecular dynamics. *Chem. Rev.* **2018,** *118* (7), 3305-3336.

38.   Chingin, K.; Balabin, R. M.; Frankevich, V.; Barylyuk, K.; Nieckarz, R.; Sagulenko, P.; Zenobi, R. Absorption of the green fluorescent protein chromophore anion in the gas phase studied by a combination of FTICR mass spectrometry with laser-induced photodissociation spectroscopy. *International Journal of Mass Spectrometry* **2011,** *306* (2), 241-245.

39.   Olsen, S.; McKenzie, R. H. A diabatic three-state representation of photoisomerization in the green fluorescent protein chromophore. *The Journal of chemical physics* **2009,** *130* (18), 05B601.

40.   Snyder Jr, J. W.; Fales, B. S.; Hohenstein, E. G.; Levine, B. G.; Martínez, T. J. A direct-compatible formulation of the coupled perturbed complete active space self-consistent field equations on graphical processing units. *The Journal of chemical physics* **2017,** *146* (17), 174113.

41.   Snyder Jr, J. W.; Curchod, B. F.; Martínez, T. J. GPU-accelerated state-averaged complete active space self-consistent field interfaced with ab initio multiple spawning unravels the photodynamics of provitamin D3. *The journal of physical chemistry letters* **2016,** *7* (13), 2444-2449.

42.   Snyder Jr, J. W.; Hohenstein, E. G.; Luehr, N.; Martínez, T. J. An atomic orbital-based formulation of analytical gradients and nonadiabatic coupling vector elements for the state-averaged complete active space self-consistent field method on graphical processing units. *The Journal of chemical physics* **2015,** *143* (15), 154107.

43.   Ufimtsev, I. S.; Martinez, T. J. Quantum chemistry on graphical processing units. 1. Strategies for two-electron integral evaluation. *Journal of Chemical Theory and Computation* **2008,** *4* (2), 222-231.

44.   Ufimtsev, I. S.; Martinez, T. J. Quantum chemistry on graphical processing units. 2. Direct self-consistent-field implementation. *Journal of Chemical Theory and Computation* **2009,** *5* (4), 1004-1015.

45.   Ufimtsev, I. S.; Martinez, T. J. Quantum chemistry on graphical processing units. 3. Analytical energy gradients, geometry optimization, and first principles molecular dynamics. *Journal of Chemical Theory and Computation* **2009,** *5* (10), 2619-2628.

46.   Seritan, S.; Bannwarth, C.; Fales, B. S.; Hohenstein, E. G.; Kokkila-Schumacher, S. I. L.; Luehr, N.; Snyder, J. W.; Song, C.; Titov, A. V.; Ufimtsev, I. S.; Martínez, T. J. TeraChem: Accelerating electronic structure and ab initio molecular dynamics with graphical processing units. *The Journal of Chemical Physics* **2020,** *152* (22), 224110.

47.   Snyder Jr, J. W.; Parrish, R. M.; Martínez, T. J. α-CASSCF: an efficient, empirical correction for SA-CASSCF to closely approximate MS-CASPT2 potential energy surfaces. *The journal of physical chemistry letters* **2017,** *8* (11), 2432-2437.

48. Shiozaki, T.; Győrffy, W.; Celani, P.; Werner, H.-J. Communication: Extended multi-state complete active space second-order perturbation theory: Energy and nuclear gradients. *The Journal of Chemical Physics* **2011,** *135* (8), 081106.

49. Kästner, J.; Carr, J. M.; Keal, T. W.; Thiel, W.; Wander, A.; Sherwood, P. DL-FIND: an open-source geometry optimizer for atomistic simulations. *The Journal of Physical Chemistry A* **2009,** *113* (43), 11856-11865.

50. Aldaz, C.; Kammeraad, J. A.; Zimmerman, P. M. Discovery of conical intersection mediated photochemistry with growing string methods. *Physical Chemistry Chemical Physics* **2018,** *20* (43), 27394-27405.

51. Aldraz, C. pyGSM. https://github.com/ZimmermanGroup/pyGSM/.

52. *BAGEL, Brilliantly Advanced General Electronic-structure Library*, http://www.nubakery.orgundertheGNUGeneralPublicLicense.

53. Shiozaki, T. BAGEL: Brilliantly Advanced General Electronic-structure Library. *Wiley Interdisciplinary Reviews: Computational Molecular Science* **2018,** *8* (1), e1331.

54. Jr., T. H. D. Gaussian basis sets for use in correlated molecular calculations. I. The atoms boron through neon and hydrogen. *The Journal of Chemical Physics* **1989,** *90* (2), 1007-1023.

55. Hack, M. D.; Wensmann, A. M.; Truhlar, D. G.; Ben-Nun, M.; Martínez, T. J. Comparison of full multiple spawning, trajectory surface hopping, and converged quantum mechanics for electronically nonadiabatic dynamics. *The Journal of Chemical Physics* **2001,** *115* (3), 1172-1186.

56. Efron, B.; Tibshirani, R. J. An introduction to the bootstrap Chapman & Hall. *New York* **1993,** *436*.

57. Efron, B. Bootstrap Methods: Another Look at the Jackknife. In *Breakthroughs in Statistics: Methodology and Distribution*, Kotz, S.; Johnson, N. L., Eds. Springer New York: New York, NY, 1992; pp 569-593.

58. Pacher, T.; Cederbaum, L. S.; Köppel, H. Approximately diabatic states from block diagonalization of the electronic Hamiltonian. *The Journal of Chemical Physics* **1988,** *89* (12), 7367-7381.

59. Cederbaum, L. S.; Schirmer, J.; Meyer, H. D. Block diagonalisation of Hermitian matrices. *Journal of Physics A: Mathematical and General* **1989,** *22* (13), 2427-2439.

60. Boys, S. F. Construction of Some Molecular Orbitals to Be Approximately Invariant for Changes from One Molecule to Another. *Reviews of Modern Physics* **1960,** *32* (2), 296-299.

61. McWeeny, R.; Coulson, C. A. The valence-bond theory of molecular structure II. Reformulation of the theory. *Proceedings of the Royal Society of London. Series A. Mathematical and Physical Sciences* **1954,** *223* (1154), 306-323.

62. Coe, J. D.; Levine, B. G.; Martínez, T. J. Ab initio molecular dynamics of excited-state intramolecular proton transfer using multireference perturbation theory. *The Journal of Physical Chemistry A* **2007,** *111* (44), 11302-11310.

63. Park, J. W.; Shiozaki, T. On-the-Fly CASPT2 Surface-Hopping Dynamics. *Journal of Chemical Theory and Computation* **2017,** *13* (8), 3676-3683.

64. Zhao, L.; Zhou, P.-W.; Li, B.; Gao, A.-H.; Han, K.-L. Non-adiabatic dynamics of isolated green fluorescent protein chromophore anion. *The Journal of Chemical Physics* **2014,** *141* (23), 235101.

65. Park, J. W.; Shiozaki, T. Analytical Derivative Coupling for Multistate CASPT2 Theory. *Journal of Chemical Theory and Computation* **2017,** *13* (6), 2561-2570.

66. Mori, T.; Martínez, T. J. Exploring the Conical Intersection Seam: The Seam Space Nudged Elastic Band Method. *Journal of Chemical Theory and Computation* **2013,** *9* (2), 1155-1163.

67. Davari, M. D.; Ferrer, F. J. A.; Morozov, D.; Santoro, F.; Groenhof, G. The lineshape of the electronic spectrum of the green fluorescent protein chromophore, part I: gas phase. *ChemPhysChem* **2014,** *15* (15), 3236-3245.

68. Farfan, C. A.; Turner, D. B. A systematic model study quantifying how conical intersection topography modulates photochemical reactions. *Physical Chemistry Chemical Physics* **2020,** *22* (36), 20265-20283.

69. Malhado, J. P.; Hynes, J. T. Non-adiabatic transition probability dependence on conical intersection topography. *The Journal of Chemical Physics* **2016,** *145* (19), 194104.

70. Dellago, C.; Bolhuis, P.; Geissler, P. L. Transition path sampling. *Advances in chemical physics* **2002,** *123*, 1-78.

71. Bolhuis, P. G.; Chandler, D.; Dellago, C.; Geissler, P. L. Transition path sampling: Throwing ropes over rough mountain passes, in the dark. *Annual review of physical chemistry* **2002,** *53* (1), 291-318.

72. Sellner, B.; Barbatti, M.; Lischka, H. Dynamics starting at a conical intersection: Application to the photochemistry of pyrrole. *The Journal of Chemical Physics* **2009,** *131* (2), 024312.

73. Conyard, J.; Heisler, I. A.; Chan, Y.; Page, P. C. B.; Meech, S. R.; Blancafort, L. J. C. s. A new twist in the photophysics of the GFP chromophore: a volume-conserving molecular torsion couple**2018,** *9* (7), 1803-1812.

74. Morozov, D.; Groenhof, G. J. A. C. Hydrogen Bond Fluctuations Control Photochromism in a Reversibly Photo-Switchable Fluorescent Protein**2016,** *128* (2), 586-588.

75. Andresen, M.; Wahl, M. C.; Stiel, A. C.; Gräter, F.; Schäfer, L. V.; Trowitzsch, S.; Weber, G.; Eggeling, C.; Grubmüller, H.; Hell, S. W.; Jakobs, S. Structure and mechanism of the reversible photoswitch of a fluorescent protein. *Proceedings of the National Academy of Sciences of the United States of America* **2005,** *102* (37), 13070.

76. Coquelle, N.; Sliwa, M.; Woodhouse, J.; Schirò, G.; Adam, V.; Aquila, A.; Barends, T. R. M.; Boutet, S.; Byrdin, M.; Carbajo, S.; De la Mora, E.; Doak, R. B.; Feliks, M.; Fieschi, F.; Foucar, L.; Guillon, V.; Hilpert, M.; Hunter, M. S.; Jakobs, S.; Koglin, J. E.; Kovacsova, G.; Lane, T. J.; Lévy, B.; Liang, M.; Nass, K.; Ridard, J.; Robinson, J. S.; Roome, C. M.; Ruckebusch, C.; Seaberg, M.; Thepaut, M.; Cammarata, M.; Demachy, I.; Field, M.; Shoeman, R. L.; Bourgeois, D.; Colletier, J.-P.; Schlichting, I.; Weik, M. Chromophore twisting in the excited state of a photoswitchable fluorescent protein captured by time-resolved serial femtosecond crystallography. *Nature Chemistry* **2018,** *10* (1), 31-37.

77. Betzig, E.; Patterson, G. H.; Sougrat, R.; Lindwasser, O. W.; Olenych, S.; Bonifacino, J. S.; Davidson, M. W.; Lippincott-Schwartz, J.; Hess, H. F. Imaging Intracellular Fluorescent Proteins at Nanometer Resolution. *Science* **2006,** *313* (5793), 1642.

78. Lin, C.-Y.; Both, J.; Do, K.; Boxer, S. G. Mechanism and bottlenecks in strand photodissociation of split green fluorescent proteins (GFPs). *Proceedings of the National Academy of Sciences* **2017,** *114* (11), E2146.

79. Romei, M. G.; Boxer, S. G. Split Green Fluorescent Proteins: Scope, Limitations, and Outlook. *Annual review of biophysics* **2019,** *48*, 19-44.